Laser-Driven Phase Segregation and Tailoring of Compositionally Graded Microstructures in Si-Ge Nanoscale Thin Films

Ozan Aktas[*,†], *Swe Z. Oo*[†,‡], *Stuart J. MacFarquhar*[†], *Vinita Mittal*[†], *Harold M. H. Chong*[‡,§], *and Anna C. Peacock*[*,†]

[†]Optoelectronics Research Centre, University of Southampton, Southampton, SO17 1BJ, UK

[‡]School of Electronics and Computer Science, University of Southampton, Southampton, SO17 1BJ, UK

[§]School of Materials Science, Japan Advanced Institute of Science and Technology, Ishikawa, 923-1292, Japan

*E-mail: O.Aktas@soton.ac.uk ; acp@orc.soton.ac.uk

Table of Contents Graphic:

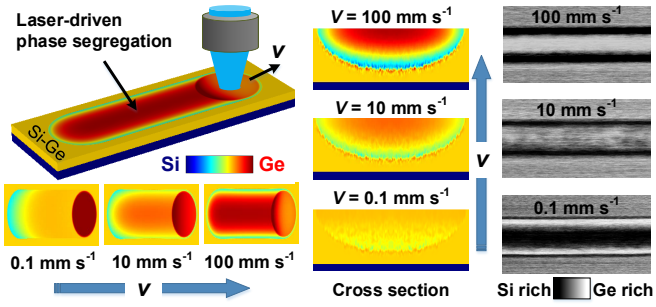

Abstract

The ability to manipulate the composition of semiconductor alloys on-demand and at nanometer-scale resolutions is a powerful tool that could be exploited to tune key properties such as the electronic bandgap, mobility, and refractive index. However, existing methods to modify the composition involve altering the stoichiometry by temporal or spatial modulation of the process parameters during material growth, limiting the scalability and flexibility for device fabrication. Here, we report a laser processing method for localized tailoring of the composition in amorphous silicon-germanium (a-SiGe) nanoscale thin films on silicon substrates, post-deposition, by controlling phase segregation through the scan speed of the laser-induced molten zone. Laser-driven phase segregation at speeds adjustable from 0.1 to 100 mm s^{-1} allows access to previously unexplored solidification dynamics. The steady-state spatial distribution of the alloy constituents can be tuned directly by setting the constant laser scan speed to achieve indefinitely long $Si_{1-x}Ge_x$ microstructures exhibiting the full range of compositions ($0<x<1$). To illustrate the potential, we demonstrate a photodetection application by exploiting the laser-written polycrystalline SiGe microstripes, showing tunability of the optical absorption edge over a wavelength range of 200 nm. Our method can be applied to pseudo-binary alloys of ternary semiconductors, metals, ceramics and organic crystals, which have phase diagrams similar to that of SiGe alloys. This study opens a route for direct laser writing of novel devices made of alloy microstructures with tunable composition profiles, including graded-index waveguides and meta-surfaces, multi-spectral photodetectors, full-spectrum solar cells, and lateral heterostructures.

Keywords: laser materials processing, semiconductor alloys, nanoscale thin films, compositionally graded microstructures, phase segregation, silicon-germanium

Lasers have been used intensively for material processing ever since their invention, owing to the ability to control their energy delivery precisely in time and space. Decades of research have culminated in the development of various laser material processing methods that can be used for crystallization, alloying, cutting, *etc*.[1,2] Recently, a new interest has emerged whereby lasers are employed to gain control over the phase segregation or transformation in liquid mixtures[3] and multi-component solids[4-6] for nanoscale manipulation of the material properties. Clearly, the ability to engineer the electrical and optical properties of semiconductor alloys in chip-based architectures at any stage of the fabrication process would be highly desirable for many applications. However, as of to date, localized control of phase segregation in semiconductor alloys using laser processing has yet to be demonstrated in nanoscale thin films on planar substrates, as the nature of the nonlinear solidification dynamics remains elusive. At present, the composition in semiconductor alloy micro/nanostructures must be controlled by temporal or spatial modulation of the process parameters over large area substrates during material growth,[7] compromising the determination over the position and orientation of the structures.

As a binary alloy, silicon-germanium (SiGe) is the simplest compound semiconductor, which makes it an ideal material to explore the capabilities of laser processing. The electronic bandgap and optical properties of $Si_{1-x}Ge_x$ can be modified by changing the composition through the Ge molar fraction x.[8] Thanks to their superior material properties such as extended mid-infrared transparency windows, low thermal conductivity, high hole and electron mobility, and complementary metal-oxide-semiconductor (CMOS) compatibility, SiGe alloys have been extensively used in a very broad range of fields, such as microelectronics,[9] optoelectronics,[10,11] thermo-photovoltaics,[12-14] synchrotron optics,[15] photonics,[16-18] and nonlinear optics.[19,20] Additionally, there is a growing interest in full-spectrum solar cells and multispectral

photodetectors, which has given impetus to the fabrication of composition-graded SiGe micro/nanostructures in both one (1D) and two-dimensional (2D) platforms.[21-24]

Over the last two decades, lasers have been applied for annealing and crystallization of amorphous SiGe thin films on glass and silicon substrates.[25-27] Up to now, laser-treated SiGe alloys have been reported to possess two laser-induced phenomena: formation of morphological surface structures,[28,29] and uncontrolled phase segregation.[30-35] SiGe alloys display a large miscibility gap in the equilibrium phase diagram, which manifests itself as strong phase segregation of Si and Ge atoms, as observed during various heat treatments.[36-38] Laser heating of the alloy creates a moving solid/liquid interface, where phase segregation occurs, producing a Ge-rich melt and a Si-rich solidified region. However, depending on the temperature gradient, constitutional undercooling can emerge, which breaks the stability of the solid/liquid interface. The interface instability results in cellular or dendritic solidification of the alloy, with a random spatial distribution of the initial overall composition.[39-41] Therefore, phase segregation of SiGe has mostly been treated in the literature as an undesired phenomenon and a challenge for material processing. Although an example of local modification of the structure and composition of a SiGe alloy using laser processing has been achieved recently in the confined geometry of a fibre,[42,43] these methods require transient effects such as acceleration or deceleration of the solidification front to be able to alter the local composition during the laser processing.

In this work, we report the results of laser crystallization and modification of the local composition in amorphous SiGe (a-$Si_{0.4}Ge_{0.6}$) nanoscale thin films deposited on c-Si planar substrates. Material characterization of the laser-melted polycrystalline $Si_{1-x}Ge_x$ regions reveals the formation of a Ge-rich strip core on the surface, surrounded by a Si-rich under-cladding. The laser-induced travelling molten zone with a curved solid/liquid interface enables the fabrication of

composition-graded microstructures over the full range of Ge molar fractions ($0<x<1$), simply by varying the laser scan speed. The observations are in excellent agreement with numerical modelling of phase segregation using finite element methods (FEM) and phase-field approaches. The potential to use these spatially graded polycrystalline SiGe microstructures for photodetection applications is demonstrated using metal-semiconductor-metal (MSM) Schottky type contacts on the laser-written microstripes, with the bandgap tunability achieved *via* the laser scan speed during processing.

Results and Discussion

Laser processing of SiGe nanoscale thin films on Si substrates

Amorphous SiGe (a-SiGe) thin films of 400 nm thickness were deposited by plasma-enhanced chemical vapour deposition (PECVD) on crystalline Si (100) wafers (see Methods). We chose an alloy composition of $Si_{0.4}Ge_{0.6}$ to leverage the large miscibility gap between the liquidus and solidus curves in the phase diagram. Here, the use of a silicon substrate offers two key benefits. Firstly, it means that our platform is immediately compatible with conventional silicon-based microelectronics, helping to facilitate convergence between photonic and electronic systems. Secondly, compared to laser processing on glass substrates[35] or within glass-clad optical fibers,[42] the higher thermal conductivity of silicon increases the range of laser scan speeds to more practical levels (>1 mm s^{-1}), enabling higher thermal gradients (~10^9 K m^{-1}), which force the solid/liquid interface instability to occur at a higher critical velocity of solidification.[44] As can be seen in the schematic of the laser processing (Figure 1a), a continuous wave (CW) argon-ion laser of 488 nm wavelength is focused on the surface of an a-SiGe thin film to create a molten zone in the alloy. High precision motorized stages are then used to move the sample, scanning the laser spot across the surface, to produce stripes of processed material (see Methods and Supporting Information

Figure S1 for the experimental setup). To help with the visual inspection of the laser-treated regions, the laser spot diameter was initially set to write 7 µm wide stripes on the surface with an optical power of 250 mW at scan speeds of 1 and 10 mm s^{-1}. The optical microscope image (Figure 1b), taken with a 100X objective and without any polarization control, shows two distinct colours at the centre of the laser-written microstripes, with darker boundaries at the edges, revealing different Ge concentrations in the Ge-rich strip cores and Si-rich under-claddings. To investigate the process at higher optical intensities, the 250 mW laser beam was then refocused to a spot diameter of 3 µm, and the speed was varied over a wider scanning range, from 0.1 mm s^{-1} up to 100 mm s^{-1}. The optical microscope image (Figure 1c) shows the highly reflective surface of the various laser-written polycrystalline SiGe (poly-SiGe) microstripes with a natural colour shading ranging from blue to yellow moving from top to bottom. These colour variations indicate a scan-speed dependent spatial redistribution of Ge concentration during solidification (see Supporting Information Figure S2 for a larger field of view).

Although the scanning electron microscope (SEM) micrograph (Figure 1d) shows similar topographical features for all of the laser-written microstripes, the back-scattered electron detector (BSED) micrograph (Figure 1e) highlights the differences in the material compositions, as the Ge-rich regions are brighter than the Si-rich regions (due to Ge's higher atomic number). Scan-speed-dependent evolution of the $Si_{1-x}Ge_x$ composition in the solidified regions is clearly visible in the magnified SEM and BSED micrographs of the microstripes written at different scan speeds, as given in Figure 1f,g for 0.1 mm s^{-1}; in Figure 1h,i for 10 mm s^{-1}; and in Figure 1k,l for 50 mm s^{-1}, respectively. For the low scan speeds, the average Ge composition is higher at both sides of the laser-written microstripes; however, it gradually accumulates at the centre for scan speeds faster than 5 mm s^{-1}. As the interaction volume (>1 µm in depth) of the back-scattered electrons is

comparable in size to those of the laser-written microstripes, BSED imaging has a limited spatial resolution, therefore it can only provide a spatially averaged $Si_{1-x}Ge_x$ composition distribution, underestimating the composition gradient.

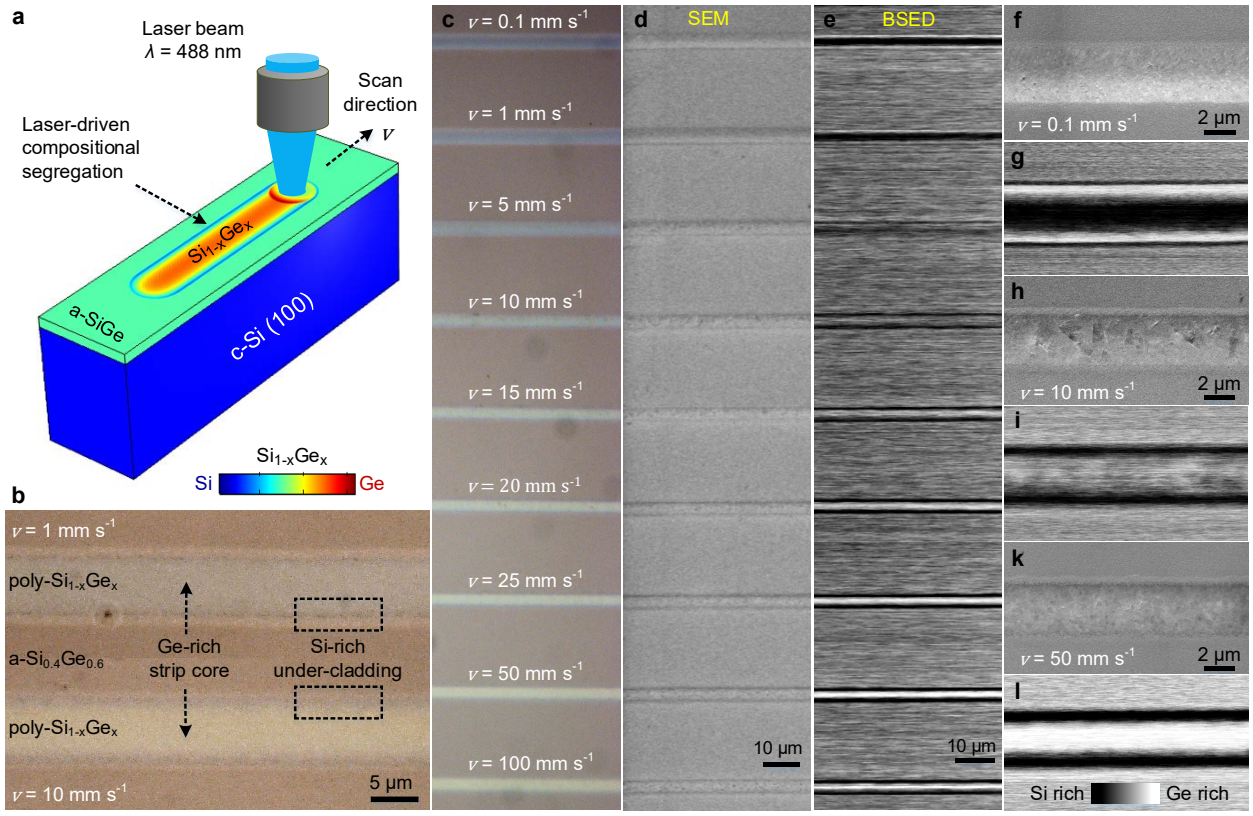

Figure 1. Laser-driven phase segregation of amorphous silicon-germanium ($a\text{-}Si_{0.4}Ge_{0.6}$) nanoscale thin films on Si substrates. **a)** Schematic of laser writing and composition redistribution after phase segregation in the SiGe thin film. **b)** Optical image of two laser-processed 7 µm wide polycrystalline SiGe (poly-SiGe) microstripes written at scan speeds 1 and 10 mm s^{-1}, as labelled, showing the Ge-rich strip core and Si-rich under-cladding regions. The difference in the natural color contrast reveals the scan-speed-dependent Ge redistribution. **c)** Optical image of 3 µm wide laser-written microstripes showing a natural color shading from blue to yellow depending on the Ge composition on the surface. **d)** SEM micrograph of the laser written microstripes displaying the topographical features of the sample surface after laser processing. **e)** Back-scattered electron detector (BSED) micrograph shows the material contrast between Ge-rich (bright) and Si-rich (dark) regions. **f)** Magnified SEM and **g)** BSED micrograph of the laser-written microstripe written at a scan speed of 0.1 mm s^{-1}. **h-l)** Same as above but for 10 mm s^{-1} (**h,i**), and 50 mm s^{-1} (**k,l**).

Investigation of laser-driven phase segregation *via* numerical simulations

We numerically investigated laser-driven phase segregation and composition redistribution during solidification by a phase-field approach,[45] running 3D FEM-based simulations (Methods). Assuming a phase-field parameter $\phi(\vec{r},t)$, which describes the laser-induced travelling molten zone with smooth transitions between the solid ($\phi = 0$) and liquid ($\phi = 1$) regions, and the SiGe alloy as a regular solution (see Supporting Information Section S1 for calculation of the phase diagram), we derived a generalized nonlinear diffusion equation (see Supporting Information Section S2) in terms of the Ge molar fraction x of $Si_{1-x}Ge_x$ as:

$$\frac{dx}{dt} = \nabla[D(\phi)\nabla x] + \nabla\left[D(\phi)(1-x)x\frac{\left[\frac{L_{Ge}}{R}\left(1-\frac{T}{T_m^{Ge}}\right)-\frac{L_{Si}}{R}\left(1-\frac{T}{T_m^{Si}}\right)+(1-2x)\left(\frac{w_L-w_S}{R}\right)\right]}{T-2(1-x)x\left[\frac{w_S}{R}(1-\phi)+\frac{w_L}{R}\phi\right]}6(1-\phi)\phi\nabla\phi\right]. \quad (1)$$

Here, $D(\phi) = D_S\,(1-\phi) + D_L\phi$ is the diffusion coefficient dependent on the solid and liquid phases; R is the ideal gas constant; $T(\vec{r},t)$ is the temperature distribution; T_m^{Ge} and T_m^{Si} are the melting temperatures of Ge and Si, respectively; L_{Ge} and L_{Si} are the latent heats of melting for Ge and Si, respectively; w_L and w_S are the regular solution parameters for liquid and solid solutions of the SiGe alloy, respectively. All regular solution parameters were determined by fitting the experimental phase diagram data of the SiGe alloy with a thermodynamically valid model (see Supporting Information Figure S3 and Table S1). Values for the material and thermal properties of the SiGe alloys were taken from the literature (Supporting Information Table S2). The second term on the right hand side of equation (1) is the phase segregation term, which drives the compositional separation of Si and Ge at the liquid/solid interface. Far from the liquid/solid interface ($\nabla\phi = 0$), equation (1) is reduced to the conventional diffusion equation in the liquid and solid regions, as expected. We solved equation (1), coupled with the time-dependent heat transfer equation, which takes the optical absorption of the laser beam as a heat source travelling at the

scan speed v. We used the experimental values for the optical power (250 mW), focused laser spot diameter (3 µm), laser scan speed range (0.1-100 mm s^{-1}), and SiGe film thickness (400 nm) in the simulations.

We estimated a maximum temperature of 1,600 ˚C on the top surface at the centre of the laser spot, which creates a molten zone with a semi-elliptical cross-section. See Supporting Information Figure S4 for the simulated temperature distribution $T(\vec{r},t)$ and the phase-field parameter $\phi(\vec{r},t)$ during laser processing. The applied optical power, which was limited to 250 mW due to the onset of surface ablation, was insufficient to melt the SiGe thin film completely. A thermal gradient of 4.5×10^{8} K m^{-1} and a cooling rate of -1.0×10^{5} K s^{-1} were estimated on the trailing edge of the travelling molten zone. The laser-induced molten zone creates compositional segregation in the alloy and becomes Ge-rich after an initial transient, which was experimentally observed during laser processing (Supporting Information Figure S5). The molten zone subsequently reaches a steady-state, dragging the Ge-rich liquid while redistributing the $Si_{1-x}Ge_x$ composition depending on the scan speed (see Supporting Information Movies S1 and S2), as illustrated in the colour composition maps given in Figure 2a-c, for the speeds 0.1, 10, and 100 mm s^{-1}, respectively. The Ge concentration builds up at the trailing edge (up to x=0.95 mol at 100 mm s^{-1}), due to insufficient diffusion-limited transport in the travelling molten zone at higher scan speeds, and solidification eventually occurs with a Ge-rich composition on the top. On the other hand, phase segregation is higher at the bottom of the molten zone than close to the top surface, due to the higher gradient $\nabla\phi$ of the phase-field parameter ϕ, resulting in a Si-rich composition deeper in the SiGe thin film. The emergence of a Ge-rich strip core and a Si-rich under-cladding in the solidified volume of the steady-state region agrees well with the experimental observations. The $Si_{1-x}Ge_x$ composition on

the lateral and longitudinal cross-sections of the steady-state region for different scan speeds can be seen in Figure 2d-f.

To simulate the averaging effect of BSED in the vertical direction, we calculated the surface-normal averaged composition in the steady-state region, by integrating the Ge molar fraction $x(\vec{r},t)$ over the spatial coordinate variable *z* from the top surface to the SiGe/c-Si interface. The simulated BSED micrographs (Figure 2g-i) show a good qualitative agreement with the experimental BSED micrographs shown in Figure 1g,i,l (see Supporting Information Figure S6 for the transverse profiles of the surface-normal averaged composition). The BSED micrographs underestimate the composition gradients, because the high Ge content in the Ge-rich strip core is compensated by the low Ge content in the Si-rich under-cladding. As shown in Figure 2k, the steady-state Ge composition *x* of the solidified material at the top surface (as extracted from Figure 2a-c) can, for example, be greater than that of the initial alloy (x_0=0.6 mol), and it can increase up to *x*=0.87 mol (87 at% Ge) at the scan speed of 100 mm s^{-1}. To make a quantitative comparison with the experimental data, we calculated volume histograms of the $Si_{1-x}Ge_x$ composition with a bin size of Δx=0.05 mol within the solidified volume in the steady-state regions for different scan speeds, which reveal the volume distributions of the Ge molar fraction $x(\vec{r},t)$ in the composition space (Figure 2l). The volume histograms can be deconvolved into two peaks by calculating the volume histograms of the composition *x* separately in the Ge-rich strip core and Si-rich under-cladding, which are divided by the isosurface of *x*=0.6 in the solidified volume, as shown for the scan speed of 100 mm s^{-1} in Figure 2m.

The simulation results suggest that our experimental observations display a solidification behaviour that is distinctly different from predictions of conventional directional solidification, where a moving planar solid/liquid interface and a diffusion-limited mixing in the molten material

are assumed.[44] The classic models predict that the solidified material has a steady-state composition equal to the initial overall average x_0, independent of the absolute value of the solidification speed v, although the phase segregation coefficient k is still affected. The steady-state composition can be altered only momentarily by acceleration or deceleration of the solidification front, modulating the power of the heating source or changing its scan speed.[42,43] However, in our case, laser heating of the alloy thin film, which induces a moving bounded molten zone with a curved interface, results in a spatially graded $Si_{1-x}Ge_x$ alloy with a steady-state composition profile determined by the absolute value of the constant laser scan speed. Steady-state Ge compositions remarkably higher and lower than the initial Ge composition x_0 can be obtained at the top surface of the strip core (Figure 2k), and at the bottom of the under-cladding, respectively.

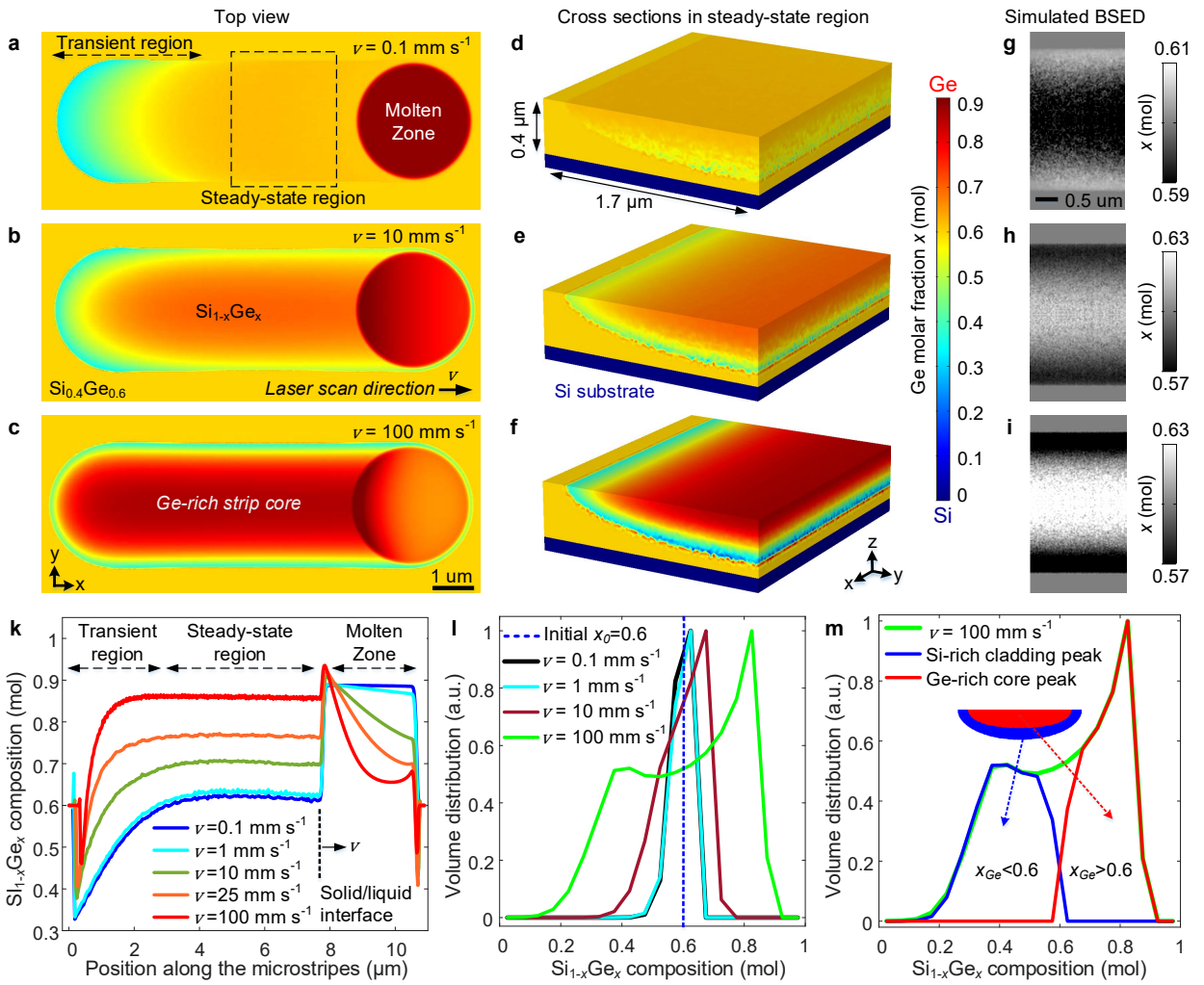

Figure 2. FEM-based phase-field simulations of laser-driven phase segregation in $Si_{0.4}Ge_{0.6}$ nanoscale thin films on Si substrates. **a-c)** Color maps show the composition of $Si_{1-x}Ge_x$ films as a spatial function of Ge molar fraction $x(\vec{r},t)$ after laser processing at the scan speeds of 0.1 mm s^{-1} (**a**), 10 mm s^{-1} (**b**), and 100 mm s^{-1} (**c**). **d-f)** Lateral and longitudinal cross-sections of the steady-state region within the laser-written microstripe is given for the speeds of 0.1 mm s^{-1} (**d**), 10 mm s^{-1} (**e**), and 100 mm s^{-1} (**f**). **g-i)** Simulated BSED micrographs (see Figure 1g,i,l for comparison) for the speeds of 0.1 mm s^{-1} (**g**), 10 mm s^{-1} (**h**), and 100 mm s^{-1} (**i**), showing the average composition of $Si_{1-x}Ge_x$ calculated in the steady-state region in the vertical direction from the top surface to the Si-substrate interface. **k)** Profiles of the Ge composition x at the center of the top surface along poly-SiGe microstripes written at different scan speeds. **l)** Volume histograms of the $Si_{1-x}Ge_x$ composition calculated within the solidified volume in the steady-state region showing the spreading of Ge molar fraction x for different laser scan speeds. **m)** Deconvolution of the volume histogram for the speed of 100 mm s^{-1} into the two peaks corresponding to the volumes of the Ge-rich strip core (red) and Si-rich under-cladding (blue), which are separated in the solidified volume of semi-elliptical cross-section by the isosurface of x = 0.6, as shown by the inset schematic.

Material characterizations of laser-written microstripes in amorphous SiGe films

We used micro-focused synchrotron X-ray diffraction (XRD) for structural analysis of the laser-written microstripes in the a-SiGe thin films (see Methods and Figure 3a for the experimental setup). The dominant XRD peak in the laser-treated regions corresponds to the (111) lattice planes, as shown in the 1D diffractograms (Figure 3b). The 2D diffractogram (Figure 3c) taken on an a-SiGe thin film processed at a scan speed of 0.1 mm s^{-1}, shows the polycrystalline nature of the laser-written microstripe with grainy XRD rings. This is expected as the SiGe film is only partially melted, down to an estimated depth of 310 nm, so that epitaxial crystal growth cannot be seeded from the c-Si substrate.[27] Application of higher powers leads to ablation of the Ge-rich top surface before full melting of the SiGe thin film can be reached. On the other hand, decreasing the thickness of the deposited SiGe film does not enable full melting either, because of the higher thermal dissipation limiting the molten depth. To overcome this restriction, longer laser wavelengths ($\lambda > 532$ nm) in the visible range could be employed to obtain deeper optical penetration in the SiGe alloy. As can be seen from the close-up view of the (111) peak in the 1D diffractogram (Figure 3d) of the SiGe microstripe written at a speed of 0.1 mm s^{-1}, it is only possible to fit the XRD data with a single peak, indicating that the compositional segregation is overshadowed by the instrument resolution. However, for scan speeds higher than 1 mm s^{-1}, there is a noticeable line broadening in the XRD rings and peaks, as displayed in the 2D and 1D diffractograms (Figure 3e,f) for a speed of 100 mm s^{-1}. The measured width of an XRD peak for an alloy is composed of various contributions, such as the crystallite size, composition gradient, strain gradient, and instrumental broadening, which makes deconvolution of the distinct components complicated. However, the peak position is determined by the mean composition in the alloy. Therefore, the appearance of the shoulder in the 1D diffractogram (Figure 3f) indicates

the formation of two distinct peaks,[37] corresponding to the Ge-rich and Si-rich regions in the laser-treated region, which can be deconvolved as shown.

1D diffractograms for the (111) peaks of the laser-written poly-SiGe microstripes are given in Figure 3g for the full range of experimental scan speeds. Fitting the peaks with pseudo-Voigt line profiles, we were able to deconvolve the Ge-rich and Si-rich peaks for each data set, except for the two lowest speeds of 0.1 and 1 mm s^{-1}. Applying Vegard's law with the formula for the d_{hkl} spacing of lattice planes given in terms of the Miller indices (h k l), we obtain equation (2) for the conversion of the (111) XRD peak positions in d-space to composition space of the Ge molar fraction x, which is given by

$$a_{SiGe}(x) = (1-x)a_{Si} + xa_{Ge} = d_{hkl}\sqrt{h^2+k^2+l^2}, \quad (2)$$

where a_{SiGe}, a_{Si} and a_{Ge} are the lattice parameters of the $Si_{1-x}Ge_x$ alloy at the deconvolved peaks in the XRD spectra, Si (5.431 Å) and Ge (5.658 Å), respectively. The $Si_{1-x}Ge_x$ compositions corresponding to the (111) peak positions of the Si-rich and Ge-rich domains are given in Figure 3h, along with the compositions of the peak positions predicted by the simulations *via* deconvolution of the volume histograms (Figure 2l,m). The instrument resolution in d_{hkl} space corresponds to a resolution of δx=0.075 mol in composition space x. However, we set the bin size as Δx=0.05 mol in the volume histograms to be able to resolve the predicted Si-rich and Ge-rich peaks for the two lowest speeds of 0.1 and 1 mm s^{-1}. The numerical results agree with the experimental XRD data up to the scan speed of 50 mm s^{-1}, after which the XRD peak positions in composition space x deviate from the predicted trend for the Si-rich and Ge-rich peaks. In our simulations, we assume that the solid/liquid interface remains stable in the experimental scan speed range. However, the critical velocity of solidification v_c for the onset of solid/liquid interface instability was estimated to be 79.9 mm s^{-1}, using predictions of solidification models (Supporting

Information Section S3). A manifestation of solidification instability was indeed encountered during the laser processing, as we observed Si-rich nanoparticles randomly dispersed within the laser-treated region at a scan speed of 100 mm s^{-1} (Supporting Information Figure S7). The critical velocity v_c is marked in Figure 3h with the vertical dashed line. We also employed X-ray fluorescence (XRF) spectroscopy to provide additional information regarding the average Ge composition in the poly-SiGe microstripes (see Methods and Supporting Information Figure S8). These narrowband measurements provide a fluorescence intensity for Ge $K\alpha_1$ emissions proportional to the amount of Ge in the $Si_{1-x}Ge_x$ thin film. The 2D XRF maps show similar Ge distributions compared to those in both the experimentally measured (Figure 1g,i,l) and numerically simulated (Figure 2g-i) BSED micrographs, helping to complete our picture of the laser-driven phase segregation in the processed microstripes.

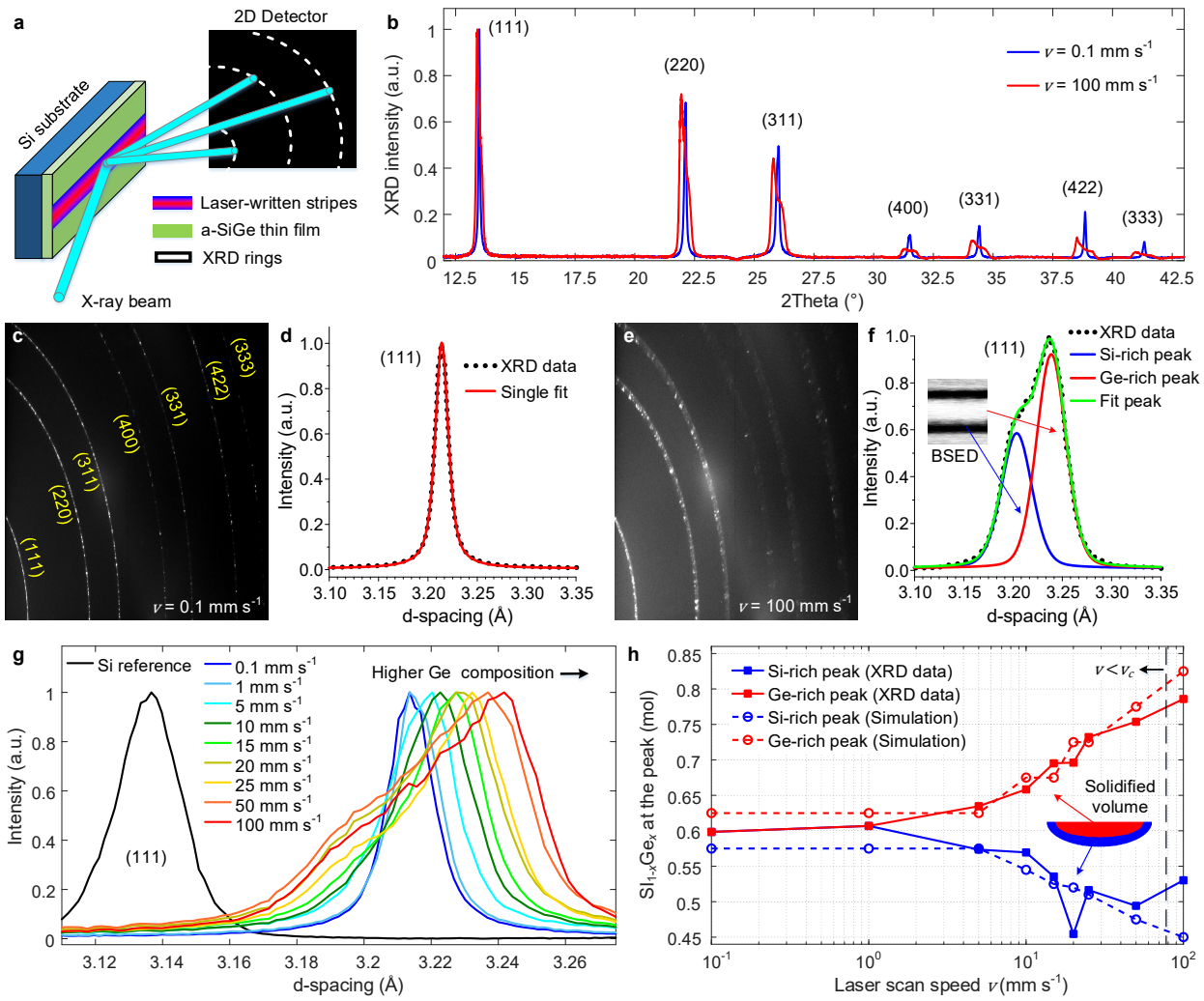

Figure 3. Micro-focus synchrotron X-ray diffraction (XRD) analysis of the laser-written poly-SiGe microstripes. **a)** Schematic of the experimental setup for the XRD measurements. **b)** 1D diffractograms show XRD peaks of different lattice planes over the experimentally accessible diffraction angles for the poly-SiGe microstripes written at speeds of 0.1 and 100 mm s^{-1}. XRD data is shown only for two scan speeds for clarity. **c)** 2D diffractogram showing XRD rings of the poly-SiGe stripe produced at a speed of 0.1 mm s^{-1}. **d)** 1D diffractogram showing only a single fit to the (111) peak, which corresponds to a small composition gradient that is insufficient to resolve against the instrument resolution. **e,f)** 2D (**e**) and 1D (**f**) diffractograms showing the effect of a larger phase segregation for laser writing at the speed of 100 mm s^{-1}. The 1D diffractogram can be resolved into two peaks corresponding to Ge-rich and Si-rich regions, as shown by the inset BSED micrograph. **g)** 1D diffractograms of the (111) peaks showing line broadening for higher scan speeds, which can be deconvolved into a Ge-rich peak and a Si-rich peak. **h)** $Si_{1-x}Ge_x$ compositions corresponding to the deconvolved peaks in the XRD data are shown along with the peak compositions predicted by simulations (see Figure 2l,m). Inset schematic shows the Si-rich (blue) and Ge-rich (red) solidified regions. The estimated critical velocity of solidification is illustrated in the figure by the dashed vertical line.

The Ge composition x close to the top surface of the laser-written poly-SiGe microstripes embedded in the 400 nm thick a-SiGe film can also be measured by using Raman spectroscopy with an excitation laser wavelength of 532 nm, which has an optical penetration depth of less than 100 nm in the Ge-rich strip cores. Figure 4a shows Raman peaks of the Ge-Ge, Si-Ge and Si-Si vibration modes taken at the centre of the top surface from the laser-written poly-SiGe microstripes processed at scan speeds of 0.1 and 25 mm s^{-1}. Measuring the shift in the experimental Raman peaks $\omega^{Si\text{-}Si}$, $\omega^{Si\text{-}Ge}$, $\omega^{Ge\text{-}Ge}$ from their unstrained positions (Supporting Information Section S4), we found that the Ge compositions are x=0.604 ±0.03 mol for 0.1 mm s^{-1}, and x=0.746±0.03 mol for 25 mm s^{-1}, which agrees with the Ge compositions estimated by the simulations (Figure 2k), and measured by the XRD (Figure 3h). By monitoring the evolution of the peak positions in the Raman spectra taken at different points across the poly-SiGe microstripes (see Figure 4b for a scan speed of 25 mm s^{-1}), we can build up a picture of the spatial profile of the Ge composition x (Figure 4c) and in-plane strain $\epsilon_{\parallel}$ (Figure 4d). The average in-plane strains across the laser-written microstripes of 0.1 and 25 mm s^{-1} are $\epsilon_{\parallel}$=0.63±0.2% and $\epsilon_{\parallel}$=0.25±0.2%, respectively. Additionally, a 2D strain analysis based on the azimuthal distortions of the XRD rings (Supporting Information Section S5 and Figure S9), was applied to the laser-written microstripes of 0.1 mm s^{-1}, where the least compositional spreading occurs. The result of the Raman spectroscopy agrees with the in-plane strain ($\epsilon_{\parallel}$=0.53%) estimated by the XRD-based strain analysis. The mismatch between the thermal expansion coefficients of the polycrystalline and amorphous SiGe materials results in residual biaxial tensile strains in the laser-processed regions, decreasing with the accumulation of the Ge-rich material on the top surface. Topographical measurements conducted using atomic force microscopy (Supporting Information Figure S10) show that the laser-treated regions have their thickness reduced by 50 nm from the amorphous film surface, due to the

densification of the poly-SiGe. Root-mean-square roughness is 2.5 nm on the surface of poly-SiGe microstripes written at the speeds of 0.1 and 1 mm s^{-1}, and this increases up to ~10 nm at the higher speeds.

As a complementary, but destructive material characterization, we used Secco wet etching to enhance the visualization of the crystalline domains. Moreover, as the etch rate is monotonously dependent on composition (being higher for the Si-rich regions), when applied to our laser processed platforms, the Si-rich under-cladding etches preferentially to suspend or fully release the Ge-rich strip cores (Supporting Information Figure S11). By controlling the etch time, it is possible to selectively release poly-SiGe microstripes of nanometre thickness with different compositions. SEM micrographs of the Secco-etched laser-written SiGe microstripes are given in Supporting Information Figure S12, which shows the under etching of the Ge-rich strip cores and removal of the Si-rich claddings.

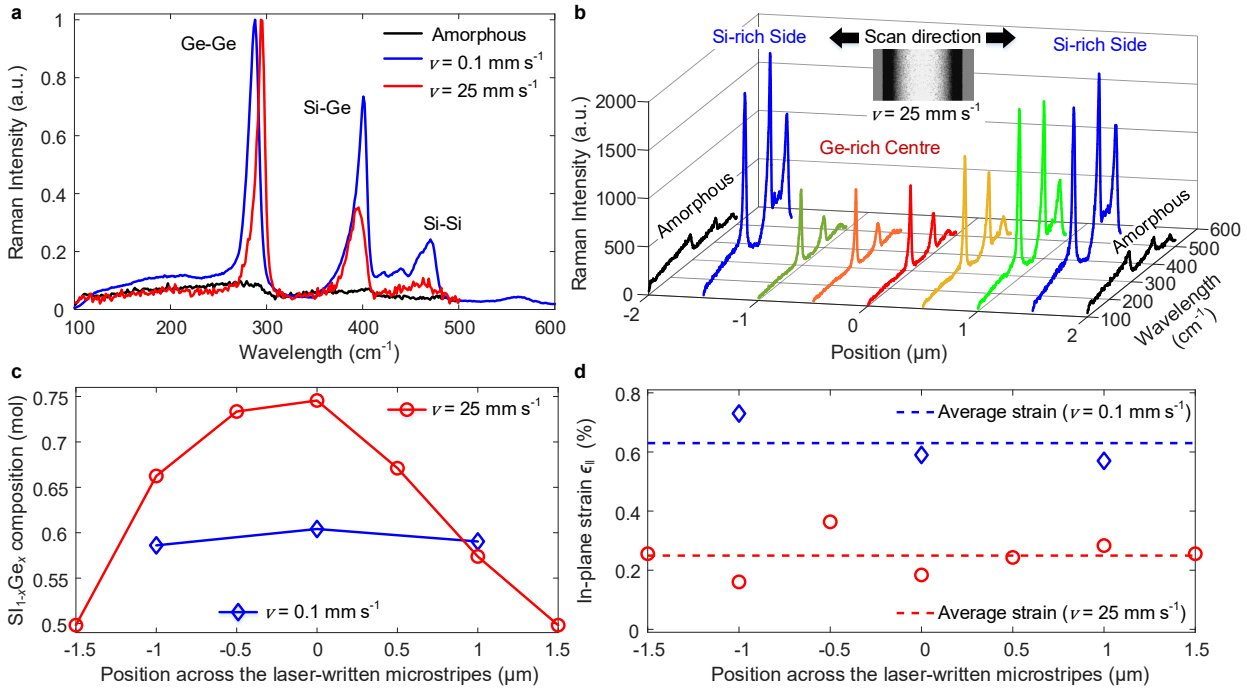

Figure 4. Micro-Raman spectroscopy of the laser-written polycrystalline SiGe microstripes. **a)** Raman spectra acquired at the center of the top surface from the poly-SiGe microstripes laser-written at scan speeds of 0.1 and 25 mm s^{-1}. Ge-Ge, Si-Ge, and Si-Si Raman peaks are indicated on the figure. The Raman spectrum taken at the surface of the non-irradiated surrounding amorphous SiGe film was rescaled to match the background profile. **b)** Raman spectroscopy measurements taken across a laser-written SiGe microstripe of 25 mm s^{-1} shows the evolution of the spectra starting from the amorphous region, through the Si-rich side to the Ge-rich center, then through the other Si-rich side to the amorphous region. The Raman intensity decreases at the center, due to the higher back reflection of the laser beam from the Ge-rich strip core. **c,d)** Spatial distribution of the Ge molar fractions x (**c**) and in-plane strains $\epsilon_{\parallel}$ (**d**) across the laser-written microstripes processed at scan speeds of 0.1 and 25 mm s^{-1}. The solid lines connecting the data points in (**c**) serve as a guide for the eye. The dashed lines in (**d**) represent the average strain values. The standard deviation in the estimation error for the Raman analysis of the composition and strain data are σ_x=0.03 mol and σ_ϵ=0.2%, respectively.

Optoelectronic characterizations of the laser-written poly-SiGe microstripes

As a proof-of-concept optoelectronic application for on-chip laser engineering of the bandgap in semiconductor alloy nanoscale thin films, we demonstrated photodetection of light with our composition-graded poly-SiGe microstripes. We tested a series of surface-normal-illuminated photoconductive detectors with metal-semiconductor-metal (MSM) contacts, by placing two stainless steel metal probes with a separation of 300 μm onto the surface of the 3 μm wide laser-written poly-SiGe stripes. Figure 5a shows the experimental configuration used for the optoelectronic characterization (Methods). An excitation laser beam of wavelength 800 nm, focused onto the surface between the two contacts, was used to generate photo-carriers, increasing the conductivity of the exposed polycrystalline region. When a voltage is applied on the probes, the system behaves as two back-to-back symmetric Schottky diodes connected with a serial resistance R that is dependent on the light intensity. The current (I)-voltage (V) characteristics, measured under dark and illuminated conditions, can be seen in Figure 5b for two poly-SiGe microstripes written with different scan speeds. The laser-written polycrystalline regions are highly conductive compared to the amorphous thin film, with a two to four orders of magnitude difference in the measured dark currents for the same contact separation (Supporting Information Figure S13). In addition, the excitation laser beam was modulated by blocking the beam at 2 second intervals and the temporal response of the photocurrent $I_{photo}=I-I_{dark}$ was recorded at a bias of V_{bias}=5V (Figure 5c). An average responsivity of 48 mA W^{-1} was achieved for both laser-written microstripes, which is close to the reported values for SiGe MSM photodetectors without any surface passivation.[10]

Spectral responsivity measurements were also conducted over the wavelength range of 980-1550 nm (Methods). The normalized detector responsivities as a function of wavelength are given in

Figure 5d. As the thickness of the deposited a-SiGe film (400 nm) is smaller than the optical penetration depth for this wavelength range, the Si substrate has a large contribution to the measured bandgap, as expected. The fundamental indirect bandgap of the unstrained $Si_{0.4}Ge_{0.6}$ alloy (Supporting Information Section S6) is $E_g^X = 0.968$ eV, which corresponds to a cut-off wavelength of 1,281 nm, as marked in Figure 5d. The residual tensile strain in the laser-written microstripes reduces the bandgap, resulting in an offset towards longer wavelengths. The spectral onset of the measurable I_{photo} of each laser-written poly-SiGe microstripe progressively shifts from the absorption edge of $Si_{0.4}Ge_{0.6}$ to longer wavelengths up to 1,500 nm, presenting a tuning range of almost 200 nm, with the increasing Ge composition on the top surface associated with the faster scan speeds. Thus, laser-driven phase segregation provides a scan-speed-dependent bandgap tunability. Although similar tunability in the bandgap has been demonstrated with $Si_{1-x}Ge_x$ nanowires[21] and $Ge_{1-x}Sn_x$ heterostructures,[46] the composition in these alloys had to be controlled during the material growth and a separate fabrication process had to be conducted for each structure, increasing the cost and complexity of future systems.

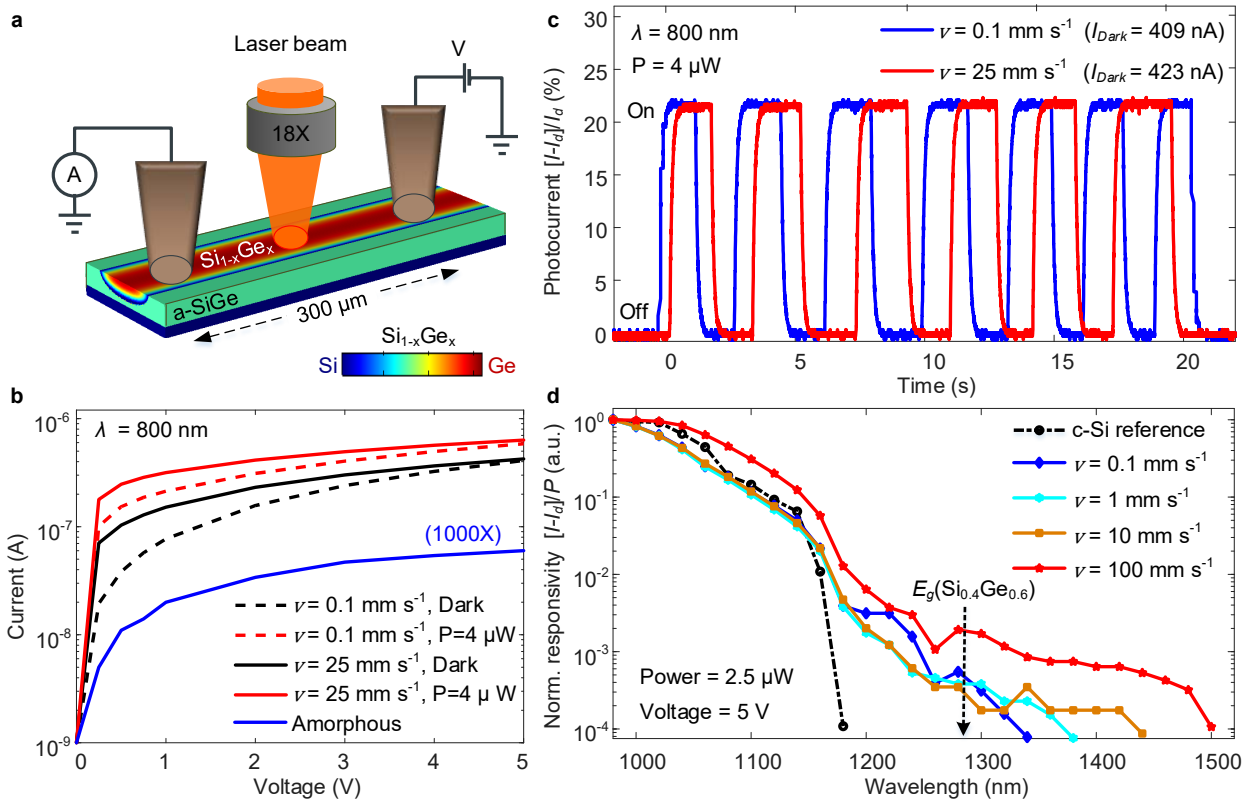

Figure 5. MSM Schottky photoconductor detectors constructed on the 3 μm wide laser-written poly-SiGe microstripes with scan-speed-tunable absorption edge. **a)** Schematic showing the experimental configuration used for the optoelectronic characterizations. The excitation laser beam was focused on the area between the Schottky contacts, which are placed 300 μm apart on the laser-written poly-SiGe microstripes. **b)** I-V characteristics taken in the dark and under illumination were measured at the Schottky contacts on poly-SiGe microstripes written at scan speeds of 0.1 and 25 mm s^{-1}. The data of the I-V measurement taken from the amorphous region with the same separation of the metal contacts was rescaled by 1000 times for visual comparison. **c)** On-off modulation of the photocurrent measured on the poly-SiGe microstripes written at 0.1 and 25 mm s^{-1} scan speeds. **d)** Normalized spectral responsivity of the photodetectors produced on the laser-written poly-SiGe microstripes with various composition profiles induced by phase segregation at different scan speeds. The spectral onset of the measurable photocurrents progressively shifts to longer wavelengths by increasing laser-writing speeds. The arrow in the figure marks the fundamental indirect bandgap E_g^X(0.968 eV) of the unstrained $Si_{0.4}Ge_{0.6}$ alloy.

Conclusions

Alternative methods exist to modify the composition spatially in semiconductor alloys either by applying elemental source and temperature gradients across a substrate during the material growth[7] or by applying stress fields on the surface after deposition.[47] However, none of these approaches can offer the flexibility of the laser processing procedure, where it is possible to control the shape, size, position, and orientation of the processed region on-demand. Such precise spatial control of the material properties opens a route for the fabrication of complex devices based on alloy microstructures such as graded-index optical waveguides and lens, meta-surfaces, Bragg gratings, laterally modulated compositional heterostructures, full-spectrum solar cells, multispectral photodetectors, and graded-base transistors, for example. The unexposed material and solute-poor under-claddings surrounding the laser-written regions can be selectively etched to release solute-rich microstripes of nanometre thickness (see Supporting Information Figure S11), which could be used for the development of micro-bolometers, thermo-electric generators, and micro-electro-mechanical (MEMS) systems, where suspended microstructures are required for thermal isolation from the substrate[48] or to allow for movement of parts.[49] Furthermore, this laser writing procedure could be applied to other multi-component material systems, including epitaxially-grown crystalline SiGe films, metal alloys (Ni–Cu, Sb–Bi), ternary semiconductors ($Al_{1-x}Ga_xAs$, $Hg_{1-x}Cd_xTe$, $Cd_{1-x}Zn_xTe$), ceramics (Al_2O_3–Cr_2O_3, V_2O_3–Cr_2O_3), and organic crystals (p-chlorobromobenzene–p-dibromobenzene), which behave as pseudo-binary systems, having isomorphous phase diagrams similar to that of SiGe alloys.[50]

In conclusion, we have shown that compositional segregation of Si and Ge in laser-processed SiGe alloys can be controlled directly *via* the scan speed and that this capability can be leveraged to modify the local optoelectronic properties of the alloys during solidification. Using

the laser-driven phase segregation in amorphous $Si_{0.4}Ge_{0.6}$ nanoscale thin films deposited on planar c-Si substrates, we produced composition-graded polycrystalline SiGe microstructures composed of Ge-rich strip cores and Si-rich under-claddings, which have steady-state Ge compositions remarkably higher and lower than the starting material, respectively. Laser writing with adjustable speeds allows for full control over the composition profile, size, and layout of the SiGe microstructures on the planar substrates. As a proof-of-principle application of lasers for bandgap engineering in the semiconductor alloys, we have demonstrated photoconductor-based detection using the laser-written SiGe microstripes and shown that the absorption edge can be tuned over a 200 nm wavelength range by simply setting the constant scan speed during laser processing. On-chip, post-deposition laser tailoring of the composition could also be applied to other multi-component material systems possessing phase diagrams similar to that of the SiGe alloys. Fabrication of embedded or suspended composition-graded alloy microstructures in nanoscale thin films could have a far-reaching impact on a wide range of applications in various fields, including microelectronics, optoelectronics, photonics, nonlinear optics, and thermo-photovoltaics.

Methods

Deposition of amorphous SiGe films on Si wafers

The silicon samples were dipped in buffered hydrofluoric acid, HF (7:1) for 3 minutes to remove the native oxide, which was followed by a quick dump rinse for 10 minutes at room temperature. The 400 nm thick a-SiGe film was deposited by plasma-enhanced chemical vapour deposition (PECVD) using the parameters: SiH_4=5 sccm, GeH_4 =50 sccm, RF=15 W, pressure=300 mTorr, temperature=200 ºC. To ensure uniform temperature across the silicon chip, the samples were preheated for 5 minutes inside the chamber.

Laser writing of polycrystalline microstripes in a-SiGe

The samples were placed on a set of high precision translation stages (Aerotech, ABL1500), which allowed for excellent positional control with adjustable speeds. The radiation source was a CW Argon ion laser operating at a wavelength of 488 nm. The beam was focused on the top surface of the sample using two different microscope objectives 10X (NA=0.25) and 20X (NA=0.40), which produced laser spots of 7 μm and 3 μm in diameter at the focus, respectively. The optical power after the objectives was set as high as possible to increase the molten zone depth in the SiGe thin film. Linear stripes of 1 cm in length were written on the sample surface with scan speeds in the range of 0.1-100 mm s^{-1}.

Micro-focus X-ray diffraction (XRD) and X-ray fluorescence (XRF) spectroscopy

We used a bright energy-tunable (2-20keV) X-ray micro-beam available at the I18 beamline of the Diamond Light Source Synchrotron Facility in Oxfordshire, UK. A focused (16.4 keV, 0.756 Å) X-ray beam with a size comparable to the width of laser-written microstripes was used to determine the structural properties of the laser-treated volume. The X-ray beam was projected on the sample surface at near grazing incidence (10°) to minimize the interaction of the beam with the Si substrate. In this geometry, the beam's footprint forms an elliptical shape with a long axis of 30 μm and a short axis of 2 μm. The long axis was aligned along the laser-written microstripes to maximize beam overlap. On the other hand, spatial resolution was maintained in the transverse direction. A single quadrant of the Debye cones for each laser-written microstripes was recorded on a 2D CMOS detector, which was positioned 117.38 mm away from the sample surface. We used a silicon standard reference (NIST-Si640D) to calibrate the diffraction ring positions in the 2D diffractograms with the DAWN Science software. The 2D diffractograms were converted into 1D diffractograms, by azimuthally integrating along the Debye rings and using a rolling ball baseline correction. For XRF mapping, Ge $K\alpha_1$ (9.886 keV) emissions were recorded on the laser-

written microstripes while scanning the sample in transverse and longitudinal directions with steps of 0.2 μm and 10 μm, respectively.

I-V and spectral responsivity measurements of photodetectors on laser-written stripes

A pulsed broadband supercontinuum laser (Fianium FemtoPower1060) with an acousto-optic tunable filter (AOTF) was used as an excitation source for I-V and spectral responsivity measurements. Optical power after the focusing objective (18X, NA-0.32) was set to 4 μW at a wavelength of 800 nm for the I-V measurements. For the spectral measurements, the optical power (2.5 μW) was calibrated at every wavelength in the range 980-1540 nm with a step size of 20 nm, by setting the RF amplitudes driving the AOFT. A c-Si wafer was used as a bandgap reference to ensure that the applied optical power was low enough that the effects of two-photon absorption had no influence on our responsivity measurements. Electrical measurements were conducted with a Keithley 2182A Nanovoltmeter and a 6221 DC current source. Metal probes were positioned on the sample surface and pushed against the laser-written microstripes until a stable dark current at a 5 V bias was recorded.

Raman spectroscopy on the laser-written poly-SiGe microstripes

Raman spectroscopy (Renishaw Invia) was applied for the complementary characterization of the laser-written poly-SiGe microstripes. The measurements were taken in the backscattered mode *via* 50X Leica objective lens (NA-0.75) using a Nd:YAG excitation laser source (532 nm, 1 mW) with a silicon grating of 2400 lines mm^{-1}. The Raman microscope can resolve the spectral features narrower than $\delta\omega$=0.5 cm^{-1} with a high spectral stability (0.02 cm^{-1}).

FEM-based phase-field simulations of laser-driven phase segregation in SiGe thin films

We used IRIDIS-5 supercomputer in the University of Southampton to run simulations in 3D with COMSOL Multiphysics software. The nonlinear diffusion equation (see equation (1)), which

was derived in Supporting Information Section S5, was solved simultaneously with the time-dependent heat transfer equations. Laser heating was modelled by using the Beer-Lambert law. The mesh size was taken as 25 nm to resolve the solid/liquid interface. Conservation of the total Ge content in the $Si_{1-x}Ge_x$ thin film was checked by calculating the volume average of x in the total volume V_{film} of the thin film, which should satisfy the condition $\int x(\vec{r},t)dV\,/V_{film} = x_0$. The instantaneous value of $x(\vec{r},t)$ at any position within the total volume was observed to always stay in the range $0 < x < 1$. Simulation parameters are given in Supporting Information Table S2.

Associated Content

Supporting Information

The Supporting Information is available free of charge on the ACS Publications website at DOI: XXXXXXXXXXXXX.

Experimental setup for laser processing, optical microscope image showing a large-area laser-processed region, theoretical calculation of SiGe phase diagram and fitting to the experimental data, derivation of the generalized nonlinear diffusion equation, simulation results for the temperature distribution and phase-field parameter, experimental observation of the initial transient region during laser processing, transverse profiles of the simulated BSED micrographs, calculation of the critical velocity of solidification, observation of Si-rich nanoparticles within the laser-written SiGe microstripes, XRF spectroscopy data, Raman analysis for the composition and strain estimation, 2D strain analysis on the XRD data, AFM data, optical microscope images and SEM micrographs after Secco wet etching, IV measurements without illumination, estimation of indirect bandgap of the unstrained $Si_{0.4}Ge_{0.6}$, video captions for simulations of the laser-driven phase segregation, tables for the experimental SiGe phase diagram data and simulation parameters.

Author Information

Corresponding Author

*E-mail: O.Aktas@soton.ac.uk

*Email: acp@orc.soton.ac.uk

Author Contributions

O.A. and A.P. conceived the research. O.A. designed the experiments, analyzed the data, and conducted the simulations and theoretical calculations. S.O. and V.M. prepared the SiGe samples under the supervision of H.C.. O.A. and S.M. performed the laser processing of the samples under the supervision of A.P.. O.A. and S.O. performed the AFM and Raman spectroscopy measurements. O.A. and S.M. performed the XRD and XRF measurements. O.A. performed the optoelectronic characterizations. O.A. and A.P. interpreted the results and wrote the manuscript. All authors contributed to the discussion and review.

Notes

The authors declare no competing financial interest.

Acknowledgments

The authors thank Prof. Sakellaris Mailis and Dr. Antoine F. J. Runge for useful discussions, and Dr. Konstantin Ignatyev of the Diamond Light Source for assistance on beamline I18 (SP17304). The authors acknowledge the use of the IRIDIS High-Performance Computing Facility at the University of Southampton, and support of the Engineering and Physical Sciences Research Council (EPSRC) (EP/P000940/1 and EP/N013247/1) in the completion of this work. The data for this work is accessible through the University of Southampton Institutional Research Repository (DOI:).

References

1. Majumdar, J. D.; Manna, I. Laser Material Processing. *Int. Mater. Rev.* **2011**, *56*, 341–388.

2. Malinauskas, M.; Zukauskas, A.; Hasegawa, S.; Hayasaki, Y.; Mizeikis, V.; Buividas, R.; Juodkazis, S. Ultrafast Laser Processing of Materials: From Science to Industry. *Light: Sci. Appl.* **2016**, *5*, e16133.

3. Walton, F.; Wynne, K. Control over Phase Separation and Nucleation Using a Laser-Tweezing Potential. *Nat. Chem.* **2018**, *10*, 506–510.

4. Choi, I.; Jeong, H. Y.; Shin, H.; Kang, G.; Byun, M.; Kim, H.; Chitu, A. M.; Im, J. S.; Ruoff, R. S.; Choi, S.-Y.; Lee, K. J. Laser-Induced Phase Separation of Silicon Carbide. *Nat. Commun.* **2016**, *7*, 13562.

5. Steele, J. A.; Yuan, H.; Ten, C. Y. X.; Keshavarz, M.; Steuwe, C.; Roeffaers, M. B. J.; Hofkens, J. Direct Laser Writing of δ- to α-Phase Transformation in Formamidinium Lead Iodide. *ACS Nano* **2017**, *11*, 8072–8083.

6. Akey, A. J.; Recht, D.; Williams, J. S.; Aziz, M. J.; Buonassisi, T. Single-Phase Filamentary Cellular Breakdown *via* Laser-Induced Solute Segregation. *Adv. Funct. Mater.* **2015**, *25*, 4642–4649.

7. Ning, C.-Z.; Dou, L.; Yang, P. Bandgap Engineering in Semiconductor Alloy Nanomaterials with Widely Tunable Compositions. *Nat. Rev. Mater.* **2017**, *2*, 17070.

8. Pethuraja, G. G.; Welser, R. E.; Sood, A. K.; Lee, C.; Alexander, N. J.; Efstathiadis, H.; Haldar, P.; Harvey, J. L. Effect of Ge Incorporation on Bandgap and Photosensitivity of Amorphous SiGe Thin Films. *Mater. Sci. Appl.* **2012**, *3*, 67–71.

9. Paul, D. J. Si/SiGe Heterostructures: From Material and Physics to Devices and Circuits. *Semicond. Sci. Technol.* **2004**, *19*, R75–R108.

10. Chen, Y. H.; Hwang, J. D.; Kung, C. Y.; Chen, P. S.; Wei, C. S.; Wu, C. K.; Liu, J. C. Improving the Performance of SiGe Metal-Semiconductor-Metal Photodetectors by Using an Amorphous Silicon Passivation Layer. *IEEE Electron Device Lett.* **2007**, *28*, 1111–1113.

11. Liu, J.; Beals, M.; Pomerene, A.; Bernardis, S.; Sun, R.; Cheng, J.; Kimerling, L. C.; Michel, J. Waveguide-Integrated, Ultralow-Energy GeSi Electro-Absorption Modulators. *Nat. Photonics* **2008**, *2*, 433–437.

12. Chiussi, S.; Serra, C.; Serra, J.; Gonzalez, P.; Leon, B.; Urban, S.; Andra, G.; Bergmann, J.; Falk, F.; Fabbri, F.; Fornarini, L.; Martelli, S.; Rinaldi, F. Laser Crystallization of Poly-SiGe for Microbolometers. *Appl. Surf. Sci.* **2002**, *186*, 166–172.

13. Hadi, S. A.; Hashemi, P.; DiLello, N.; Polyzoeva, E.; Nayfeh, A.; Hoyt. J. L. Thin-Film $Si_{1-x}Ge_x$ HIT Solar Cells. *Sol. Energy* **2014**, *103*, 154–159.

14. Taborda, J. A. P.; Romero, J. J.; Abad, B.; Munoz-Rojo, M.; Mello, A.; Briones, F.; Martin Gonzalez, M. S. Low Thermal Conductivity and Improved Thermoelectric Performance of Nanocrystalline Silicon Germanium Films by Sputtering. *Nanotechnology* **2016**, *27*, 175401.

15. Erko, A.; Abrosimov, N. V.; Alex, V. Laterally-Graded SiGe Crystals for High Resolution Synchrotron Optics. *Cryst. Res. Technol.* **2002**, *37*, 685–704.

16. Schmidtchen, J.; Schuppert, B.; Petermann, K. Passive Integrated-Optical Waveguide Structures by Ge-Diffusion in Silicon. *J. Lightwave Technol.* **1994**, *12*, 842–848.

17. Ramirez, J. M.; Vakarin, V.; Frigerio, J.; Chaisakul, P.; Chrastina, D.; Le Roux, X.; Ballabio, A.; Vivien L., Isella, G.; Marris-Morini, D. Ge-rich Graded-Index $Si_{1-x}Ge_x$ Waveguides with Broadband Tight Mode Confinement and Flat Anomalous Dispersion for Nonlinear Mid-Infrared Photonics. *Opt. Express* **2017**, *25*, 6561–6567.

18. Chaisakul, P.; Marris-Morini, D.; Frigerio, J.; Chrastina, D.; Rouifed, M.-S.; Cecchi, S.; Crozat, P.; Isella, G.; Vivien, L. Integrated Germanium Optical Interconnects on Silicon Substrates. *Nat. Photonics* **2014**, *8*, 482–488.

19. Ettabib, M. A.; Xu, L. ; Bogris, A. ; Kapsalis, A.; Belal, M.; Lorent, E.; Labeye, P. ; Nicoletti, S.; Hammani, K.; Syvridis, D.; Shepherd, D. P.; Price, J. H. V.; Richardson, D. J.; Petropoulos, P. Broadband Telecom to Mid-Infrared Supercontinuum Generation in a Dispersion-Engineered Silicon Germanium Waveguide. *Opt. Lett.* **2015**, *40*, 4118–4121.

20. Yang, C.-C.; Cheng, C.-H.; Chen, T.-H.; Lin, Y.-H.; Chi, Y.-C.; Tseng, W.-H.; Chang, P.-H.; Chen, C.-Y.; Chen, K.-H.; Chen, L.-C.; Wu, C.-I.; Lin. G.-R. Ge-rich SiGe Mode-Locker for Erbium-Doped Fiber Lasers. *IEEE J. Sel. Top. Quantum Electron.* **2018**, *24*, 1100310.

21. Kim, C.-J.; Lee, H.-S.; Cho, Y.-J.; Yang, J.-E.; Lee, R. R.; Lee, J. K.; Jo, M.-H. On-Nanowire Band-Graded Si:Ge Photodetectors. *Adv. Mater.* **2011**, *23*, 1025–1029.

22. Matsumura, R.; Tojo, Y.; Kurosawa, M.; Sadoh, T.; Mizushima, I.; Miyao, M. Growth-Rate-Dependent Laterally Graded SiGe Profiles on Insulator by Cooling-Rate Controlled Rapid-Melting-Growth. *Appl. Phys. Lett.* **2012**, *101*, 241904.

23. Gontad, F.; Conde, J. C.; Chiussi, S.; Serra, C.; González, P. 193 nm Excimer Laser Processing of Si/Ge/Si(100) Micropatterns. *Appl. Surf. Sci.* **2016**, *362*, 217–220.

24. Littlejohns, C. G.; Bucio, T. D.; Nedeljkovic, M.; Wang, H.; Mashanovich, G. Z.; Reed, G. T.; Gardes, F. Y. Towards a Fully Functional Integrated Photonic-Electronic Platform *via* a Single SiGe Growth Step. *Sci. Rep.* **2016**, *6*, 19425.

25. Sedky, S.; Schroeder, J.; Sands, T.; King, T.-J.; Howe, R. T. Effect of Excimer Laser Annealing on the Structural Properties of Silicon Germanium Films. *J. Mater. Res.* **2004**, *19*, 3503–3511.

26. Sameshima, T.; Watakabe, H.; Kanno, H.; Sadoh, T.; Miyao, M. Pulsed Laser Crystallization of Silicon-Germanium Films. *Thin Solid Films* **2005**, *487*, 67–71.

27. Ong, C. Y.; Pey, K. L.; Ong, K. K.; Tan, D. X. M.; Wang, X. C.; Zheng, H. Y.; Ng, C. M.; Chan, L. A Low-Cost Method of Forming Epitaxy SiGe on Si Substrate by Laser Annealing. *Appl. Phys. Lett.* **2009**, *94*, 082104.

28. Weizman, M.; Nickel, N. H.; Sieber, I.; Yan, B. Laser-Induced Self-Organization in Silicon-Germanium Thin Films. *J. Appl. Phys.* **2008**, *103*, 093536.

29. Qi, D.; Li, X.; Wang, P.; Chen, S.; Huang, W.; Li, C.; Huang, K.; Lai, H. Evolution of Laser-Induced Specific Nanostructures on SiGe Compounds *via* Laser Irradiation Intensity Tuning. *IEEE Photonics J.* **2014**, *6*, 2200005.

30. Brunco, D. P.; Thompson, M. O.; Hoglund, D. E.; Aziz, M. J.; Gossmann, H.-J. Germanium Partitioning in Silicon during Rapid Solidification. *J. Appl. Phys.* **1995**, *78*, 1575–1582.

31. Ong, C. Y.; Pey, K. L.; Li, X.; Wang, X. C.; Ng, C. M.; Chan, L. Laser Annealing Induced High Ge Concentration Epitaxial SiGe Layer in $Si_{1-x}Ge_x$ Virtual Substrate. *Appl. Phys. Lett.* **2008**, *93*, 041112.

32. Runge, A. F. J., Franz, Y,; Littlejohns, C. G.; Grabska, K.; Mailis, S.; Gardes, F. Y.; Peacock, A. C. Laser-Assisted Material Composition Engineering of SiGe Planar Waveguides. CLEO-Pacific Rim: Singapore, 2017(https://eprints.soton.ac.uk/415700).

33. Chiussi, S.; Lopez, E.; Serra, J.; Gonzalez, P.; Serra, C.; Leon, B.; Fabbri, F.; Fornarini, L.; Martelli, S. Influence of Laser Fluence in ArF-Excimer Laser Assisted Crystallization of a-SiGe:H Films. *Appl. Surf. Sci.* **2003**, *208-209*, 358–363.

34. Weizman, M.; Nickel, N. H.; Sieber, I.; Yan, B. Successive Segregation in Laser-Crystallized Poly-SiGe Thin Films. *J. Non-Cryst. Solids* **2006**, *352*, 1259–1262.

35. Kitahara, K.; Hirose, K.; Suzuki, J.; Kondo, K.; Hara, A. Growth of Quasi-Single-Crystal Silicon-Germanium Thin Films on Glass Substrates by Continuous Wave Laser Lateral Crystallization. *Jpn. J. Appl. Phys.* **2011**, *50*, 115501.

36. Abrosimov, N. V.; Rossolenko, S. N.; Thieme, W.; Gerhardt, A.; Schröder, W. Czochralski Growth of Si- and Ge-rich SiGe Single Crystals. *J. Cryst. Growth* **1997**, *174*, 182–186.

37. Mogaddam, N. A.; Alagoz, A. S.; Yerci, S.; Turan, R.; Foss, S.; Finstad, T. G. Phase Separation in SiGe Nanocrystals Embedded in SiO_2 Matrix During High Temperature Annealing. *J. Appl. Phys.* **2008**, *104*, 124309.

38. Kinoshita, K.; Miyata, H.; Tanaka, R.; Ueda, T.; Arai, Y.; Yoda, S. $Si_{0.5}Ge_{0.5}$ Bulk Single Crystals with Uniform Composition. *J. Cryst. Growth* **2012**, *349*, 50–54.

39. Mokhtari, M.; Fujiwara, K.; Takakura, G.; Maeda, K.; Koizumi, H.; Nozawa, J.; Uda, S. Instability of Crystal/Melt Interface in Si-Rich SiGe. *J. Appl. Phys.* **2018**, *124*, 085104.

40. Gotoh, R.; Fujiwara, K.; Yang, X.; Koizumi, H.; Nozawa, J.; Uda, S. Formation Mechanism of Cellular Structures During Unidirectional Growth of Binary Semiconductor Si-Rich SiGe Materials. *Appl. Phys. Lett.* **2012**, *100*, 021903.

41. Yang, X.; Fujiwara, K.; Abrosimov, N. V.; Gotoh, R.; Nozawa, J.; Koizumi, H.; Kwasniewski, A.; Uda, S. The Critical Growth Velocity for Planar-to-Faceted Interfaces Transformation in SiGe Crystals. *Appl. Phys. Lett.* **2012**, *100*, 141601.

42. Coucheron, D. A.; Fokine, M.; Patil, N.; Breby, D. W.; Buset, O. T.; Healy, N.; Peacock, A. C.; Hawkins, T.; Jones. M.; Ballato, J.; Gibson, U. J. Laser Recrystallization and Inscription of Compositional Microstructures in Crystalline SiGe-Core Fibres. *Nat. Commun.* **2016**, *7*, 13265.

43. Gumennik, A.; Levy, E. C.; Grena, B.; Hou, C.; Rein, M.; Abouraddy, A. F.; Joannopoulos, J. D.; Fink, Y. Confined in-Fiber Solidification and Structural Control of Silicon and Silicon-Germanium Microparticles. *Proc. Natl. Acad. Sci. U. S. A.* **2017**, *114*, 7240–7245.

44. Kurz, W.; Fisher, D. J. Fundamentals of Solidification; Trans Tech Publications: Aedermannsdorf, 1992; Ch.3.

45. La Magna, A.; Alippi, P.; Privitera, V.; Fortunato, G.; Camalleri, M.; Svensson, B. A Phase-Field Approach to the Simulation of the Excimer Laser Annealing Process in Si. *J. Appl. Phys.* **2004**, *95*, 4806–4814.

46. Gassenq, A.; Gencarelli, F.; Campenhout, J. V.; Shimura, Y.; Loo, R.; Narcy, G.; Vincent, B.; Roelkens, G. GeSn/Ge Heterostructure Short-Wave Infrared Photodetectors on Silicon. *Opt. Express* **2012**, *20*, 27297.

47. Ghosh, S.; Kaiser, D.; Bonilla, J.; Sinno, T.; Han, S. M. Stress-Directed Compositional Patterning of SiGe Substrates for Lateral Quantum Barrier Manipulation. *Appl. Phys. Lett.* **2015**, *107*, 072106.

48. Goyal, C. P.; Omprakash, M.; Navaneethan, M.; Takeuchi, T.; Shimura, Y.; Shimomura, M.; Ponnusamy, S.; Hayakawa, Y.; Ikeda, H. Fabrication of Ultrathin Poly-Crystalline SiGe-on-Insulator Layer for Thermoelectric Applications. *J. Phys. Commun.* **2019**, *3*, 075007.

49. Sedky, S. SiGe: An Attractive Material for Post-CMOS Processing of MEMS. *Microelectron. Eng.* **2007**, *84*, 2491–2500.

50. Liang, L. H.; Liu, D.; Jiang, Q. Size-Dependent Continuous Binary Solution Phase Diagram. *Nanotechnology* **2003**, *14*, 438–442.